Aqueous tape casting of microwave ceramic BaO • La$_2$O$_3$ • 4.7TiO$_2$

CHENG CHUNG LEE, PANG LIN
Institute of Materials Science and Engineering, National Chiao Tung University, Hsinchu, Taiwan
E-mail: lecc@erso.itri.org.tw

An aqueous-based slip for tape-casting BaO • La$_2$O$_3$ • 4.7TiO$_2$ ceramic sheets was studied that is suitable for substrates of microwave devices. Two separate dispersants, Na$_4$P$_2$O$_7$ (S2) and CH$_3$(CH$_2$)$_4$SO$_3$Na, combined with poly(vinyl alcohol) and poly(ethylene glycol), were used as slip additives. The zeta potential, particle size distribution, viscosity (of the slip), tensile strength and density (of green tapes), sintered density, microstructures and microwave dielectric properties (of sintered substrates) were characterized, and their dependence on the additives were analysed. S2 shows a better dispersion function and leads to a higher density of the tapes. During the sintering, the S2 liquid on grain boundaries hindered the grain growth and the formation of second phase. The dispersant-dependent microstructures of the substrates show strong influences on the dielectric properties.

1. Introduction

Tape casting is a well-established technique for making large-area, flat, laminated ceramics, which have found wide applications in various fields of the electronics industry. Based on this technique, ceramic substrates and multilayered structures of several materials, such as substrates of Al$_2$O$_3$ [1–3] for thick- and thin-film circuitry; and multilayers of BaTiO$_3$ for capacitors [4], have been fabricated. Similar layered-structure ceramics were utilized in microwave passive components for communications. While a variety of microwave ceramics in bulk form have been extensively investigated [5–8], the related tape-casting process is rarely reported. In addition, the flammability and toxicity associated with the organic solvents, which are frequently used as a liquid vehicle in the conventional process, have received increasing attention and motivated the study of aqueous-based tape-casting systems to meet the environmental requirements [9–11].

We report the development of an aqueous-based slip for tape casting of BaO • La$_2$O$_3$ • 4.7TiO$_2$ ceramics that is suitable for the substrates used in microwave devices. Detailed microwave dielectric properties and micro-structures of these ceramics have been presented previously [12]. The experiments reported here concentrate on the slurry formulation and its effects on the physical properties of the slips, green tapes and sintered substrates. Binder and plasticizer loading were optimized with respect to mechanical properties and density of the tapes. Two frequently used dispersants, methyl sulfonic acid sodium salt (D1: CH$_3$(CH$_2$)$_4$SO$_3$Na, organic type) and sodium pyrophospate (S2: Na$_4$P$_2$O$_7$ inorganic type), were tested and their overall performance was evaluated.

2. Experimental
2.1. Preparation of the slurry, tapes, laminates and substrates

A typical composition of the tape-casting slip is shown in Table I. Ceramic powder was prepared from reagent-grade BaCO$_3$, La$_2$O$_3$ and TiO$_2$. The raw materials were mixed according to the ratio BaO: La$_2$O$_3$:TiO$_2$ = 1 : 1 : 4.7, ball milled (with ZrO$_2$ milling media) for 16 h, calcined at 1000 °C in air for 4 h, milled again for 20 h to reduce the particle size and then dried with a lamp. Dispersant was dissolved in the deionized water and then fully mixed with the ceramic powder to yield an aqueous suspension, which was subsequently added with the binder poly(vinyl alcohol) (PVA) and plasticizer poly(ethylene glycol) (PEG) to form a viscous slip.

The slip was vacuum degassed and forced through a 200 mesh nylon to remove any large particles or undissolved binder, if present. It was then cast (17 cm min^{-1}), using a two-blade casting head, onto a polyester film (Mylar). After drying for 12 h, the tapes (300–400 µm in thickness) were peeled off the film and cut to the desired shape for subsequent measurements. Laminates (550–700 µm) were prepared from the dried tapes by stacking two layers and hot pressing them with a pressure of 88 MPa at 100 °C for 30 min. The laminates were then sintered at 1350 °C in air for 0.5–4 h to yield ceramic substrates of size ∼ 50 mm × 50 mm and thickness ∼ 370–500 µm.

In this work, two series of slip, L1 and L2, were used in most of the experiments (except in section 3.1.), where the contents of L1 are ceramic powder (50 wt %), D1(1.5 wt %) or S2(0.5 wt %), PVA(10 wt %),

TABLE I Composition of slurry for tape casting

Component	Function	Composition (wt %)
BaO-La$_2$O$_3$-4.7TiO$_2$	Ceramic Powder	50
Deionized water	Solvent	42.5–28.25
Polyvinyl alcohol (PVA)*	Binder	5–12.5
Poly(ethylene glycol) (PEG)◆	Plasticizer	2.5–6.25
1-pentane sulfonic acids Sodium salt (D1)†	Dispersant	0–3.0
Sodium pyrophosphate (S2)★	Dispersant	0–3.0

*Showa chemicals, Inc. Tokyo, Japan. ◆Riedel-de haën AG-D-30926 Germany.
†Tokyo kasei kogyo Co., Ltd. Tokyo, Japan. ★Fairfiew, Ohio 45014 USA.

PEG(x wt %) and deionized water; L2 series have the same contents as that of L1 except the PVA(y wt %) and PEG($0.5y$ wt %). The range of x varies from 0 to 10, and y from 5 to 12.5.

2.2. Measurements

The phases of the ceramic powder and the sintered substrates were identified using X-ray diffraction (XRD) with CuK$_\alpha$ radiation. The zeta potential (ζ) and the particle size distribution of suspensions of ceramic powder in water were measured using a zeta potential analyser (Brookhaven, Inc; Zetaplus) and a particle size analyser (Coulter Fluid Module; LS 320), respectively. The viscosity measurements of slurry were carried out using a viscometer (Weissenberg rheogoniometer). The tensile strength and strain to failure of green tapes were measured on dog-bone-shaped tape specimens at a loading rate of 5.0 mm min^{-1} using a universal testing machine. The density of green tapes was estimated based on the ratio of weight/volume for 15–20 disk samples (6.5 mm in diameter) punched from a given tape. The density of sintered substrates was measured using the Archimedes method. The microstructures of relevant samples were observed using scanning electron microscopy (SEM). Quantitative analysis of the compositions of sintered substrates was carried out using a wavelength dispersive X-ray spectrometer (WDS). The microwave properties of the substrates were determined based on the rectangular cavity method (M1202 RECT and software CAVITY v6.2, Damaskos). The sample was placed in the center of the cavity, in which the transmission mode resonance occurred in the TE$_{10n}$ modes ($n \geq 1$) where the electric field is perpendicular to the top and bottom plates and the magnetic field is circumferential. Detailed measurement procedures have been described elsewhere [13].

3. Results and discussions
3.1. Dispersion of ceramic powder

Aqueous suspensions of ceramic powder, without the addition of any binder and plasticizer, were prepared to study the dispersion effects. The zeta potential of the suspensions is displayed as a function of pH value in Fig. 1. The suspension pH was adjusted by addition of either 1 M HNO$_3$ or 1 M NH$_4$. In the case without dispersant added, the isoelectric point (IEP) where $\zeta = 0$ has a
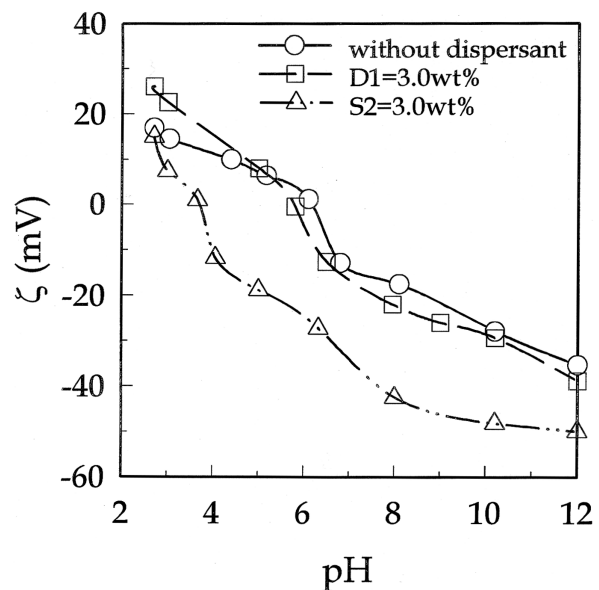
Figure 1 Zeta potential versus pH for the aqueous suspension of BaO • La$_2$O$_3$ • 4.7TiO$_2$ ceramic powder without the addition of any binder and plasticizer.

pH $= 6.2$. The IEP has a minor shift to pH $= 5.8$ when dispersant D1 (3 wt %) was added, and a significant IEP change to pH $= 3.6$ was observed with the addition of S2 (3 wt %).

The ζ behaviour of the suspension can be understood in terms of a surface layer of the metal hydroxide which is amphoteric in nature [14]. The IEP indicates a zero electrokinetic charge on the oxide particles in the aqueous solution. In acidic solution, the oxide surfaces tend to be positively charged through excess adsorption of hydrogen ions to the hydroxyl group (MOH + H$^+ \rightarrow$ MOH$_2^+$), while in basic solution the charge tends to be negative due to the excess OH$^-$ adsorption (MOH + OH$^- \rightarrow$ MO + H$_2$O) to make the ζ negative.

In the suspensions with D1 and S2 the shift of IEP to the lower pH may arise from the adsorption of dispersant anions to oxide surface, which consequently decreases the ζ potential at a particular pH level. The extent of shift indicates the relative tendency of the adsorption.

The effects of dispersant concentration on ζ (pH $= 8.0$), tested in a wide range, was shown in Fig. 2. The ζ value exhibits a rapid decline to a large negative potential ~ -50 mV as S2 concentration increases up to 4 wt %, showing the steady absorption of anions to make the potential increasing negative. The following mild decrease of ζ with the concentration (until ~ 9 wt %) indicates the adsorption approaching saturation. Beyond that, the double layer extension around the oxide surface is compressed by the highly concentrated electrolyte, leading to the potential reducing in magnitude to nearly zero. In contrast, the ζ potential only shows a weak change through the entire range of D1 concentration. It remains at less than 25 mV in magnitude, which is the minimum requirement of ζ for a stable suspension at room temperature. The corresponding particle size distribution (Fig. 3a) reveals a minor dispersing effect of D1 due to its weak electrostatic repulsive force among the particles in the suspension.

The size distribution analysis (Fig. 3b) proves S2 to be an effective dispersant at a loading ≥ 0.5 wt %. Large
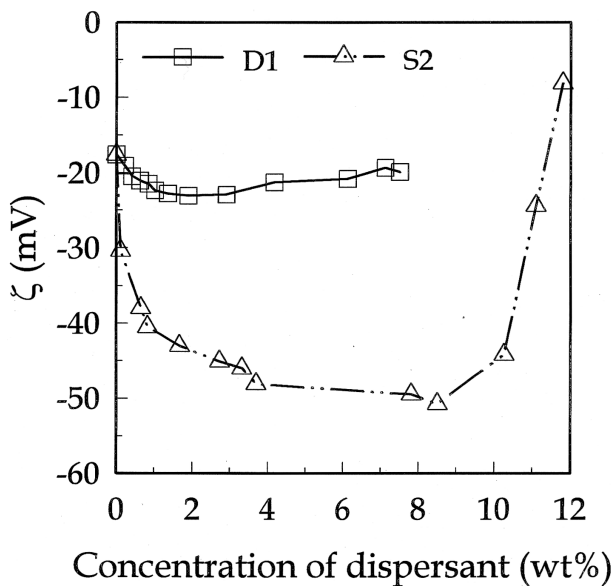
Figure 2 Zeta potential versus concentration of dispersants for the same aqueous suspension as Fig. 1 with pH = 8.0.
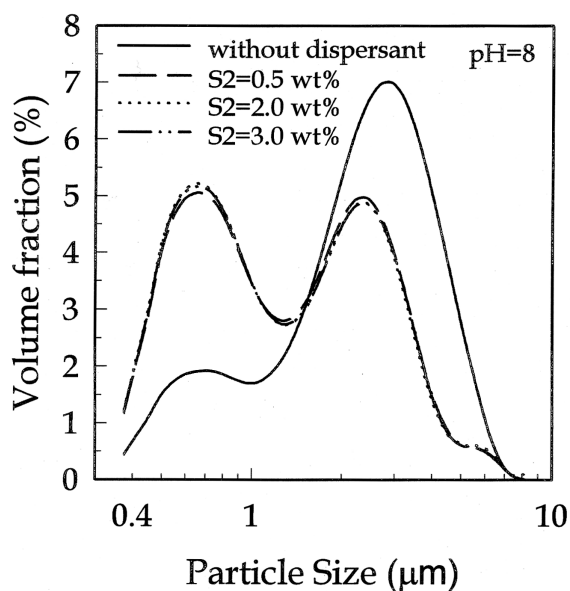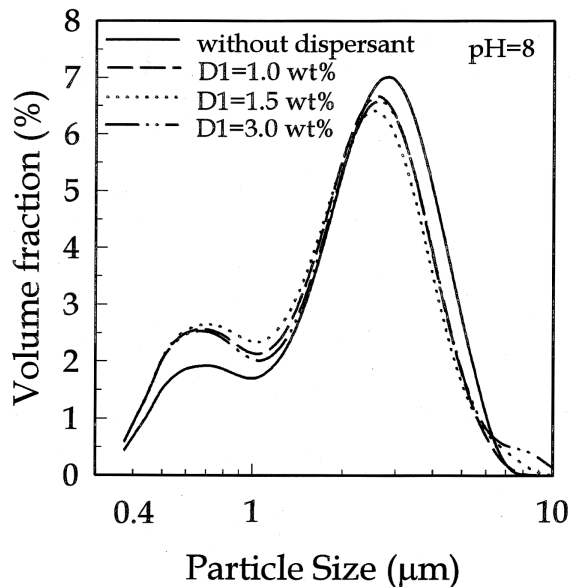

Figure 3 Particle size distribution of the same aqueous suspension as Fig. 1, which were added with various amount of dispersant (a) D1 and (b) S2.

flocculated particles were dispersed into small ones, which formed a component (< 1.2 μm) distinct from the other one (> 1.2 μm). The two major components of particles were separated physically using a gravity-sedimentation process. The suspension was poured slowly into a glass tube, which was pre-filled with water to half height. As the dispersion settled, the upper cloudy liquid was collected and dried to obtain the submicrometer component. The other component was gathered from the dense sediment.

XRD studies shows that the submicrometer component consists mainly of $La_2Ti_2O_7$ and the other component is mostly $BaTi_4O_9$ (Fig. 4a and b). The size disparity of the two phases may be ascribed to either their different growth rates during calcination or their different resistance to fracture when subjected to ball-milling impact. Minor $BaLa_2Ti_4O_{12}$ peaks are also present in the XRD pattern, which is the main phase when sintering is carried out up to 1300 ℃ (see Section 3.6.). NaOH•H₂O, found in the residual of the dried cloudy liquid, is the precipitate of hydrated crystals consisting of the cations (Na^+) of the dissolved S2.

3.2. Rheology of slurry

The apparent viscosity as a function of shear rate for the slips L1 and L2 are shown in Fig. 5a and b, where D1 was used as the dispersant. Similar rheology behaviours were observed in the slips added with S2 and not shown here. The viscosity of L1 series shows a decrease with increasing plasticizer (Fig. 5a), which acts to reduce the glass-transition temperature T_g of the binder [15].

Since the viscosities usually range from 1–5 Pa s for standard tape formulation [3], the slip L1 with a PEG content around 7.5 wt % would give an adequate viscosity in the wide shear rate range $0–600\,s^{-1}$ for an ordinary tape-casting process.

It is noted that the viscosity curves follow a Bingham plastic pattern until a critical shear rate where they increase again, similar to a shear-thickening behaviour.
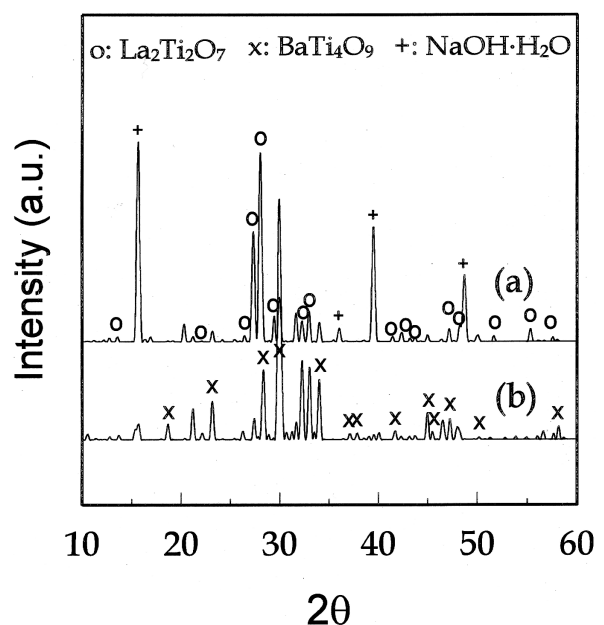

Figure 4 XRD patterns of the ceramic powder showing the components with a size (a) < 1.2 μm and (b) > 1.2 μm.
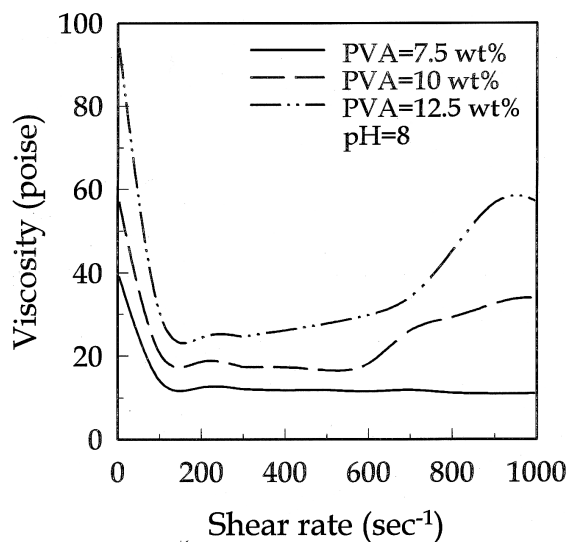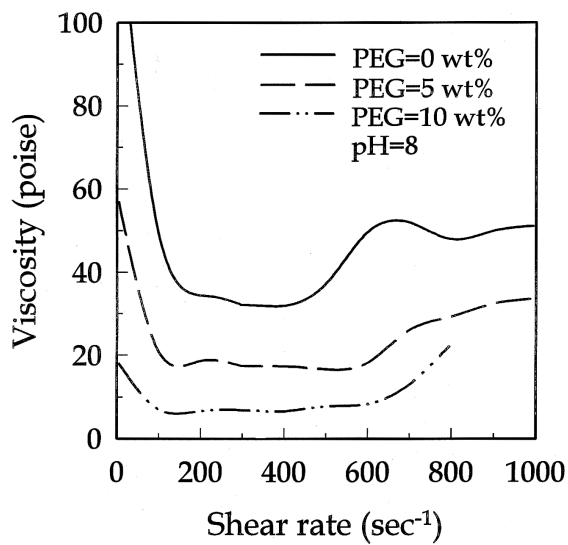
411

Figure 5 Effect of (a) PEG addition on the viscosity behaviour of L1 slip and (b) PVA addition on the viscosity behaviour of L2 slip. Both slips were added with D1.

Figure 6 SEM micrographs of L1 slip after a rheology test with (a) a low shear rate $\sim 200\,\mathrm{s}^{-1}$ and (b) a high shear rate $\sim 800\,\mathrm{s}^{-1}$.

This behaviour is attributed to severe cross-linking of PVA chains, which occurred during the high-rate shearing test. The cross-linking is an irreversible process where an initially uniform, well dispersed slip (Fig. 6a) was transformed radically into a slurry with a locally aggreagated network structure (Fig. 6b). The PEG molecules, presumably being mixed with PVA chains and blocking the interaction between the chains, could reduce the cross-linking probability and hinder the irreversible process unless the higher shear rate was applied. Therefore, the critical shear rate (~ 500–$700\,\mathrm{s}^{-1}$) is seen to increase with the PEG content. Further evidence is shown in Fig. 5b, where the shear-thickening behaviour reduces with a decreasing amount of PVA involved in slip L2 series. An almost constant viscosity can be achieved beyond a shear rate of $100\,\mathrm{s}^{-1}$ at a PVA content of 7.5 wt %.

3.3. Tensile strength of green tapes

The tensile stress and strain to failure of the green tapes cast from slip L1 series are illustrated in Fig. 7. The stress/strain curves of the tapes added with D1 are similar to those of tapes added with S2 except that the curves of
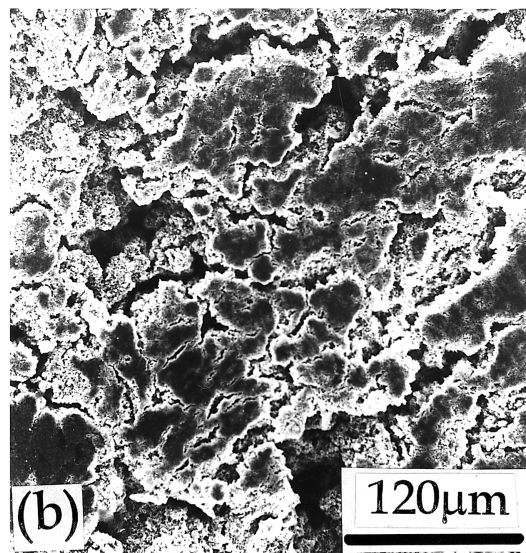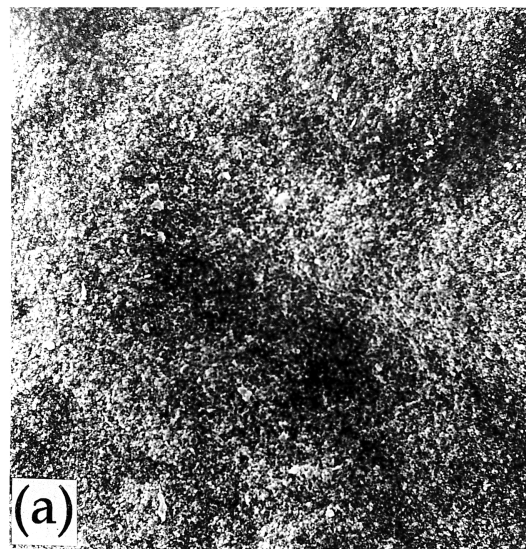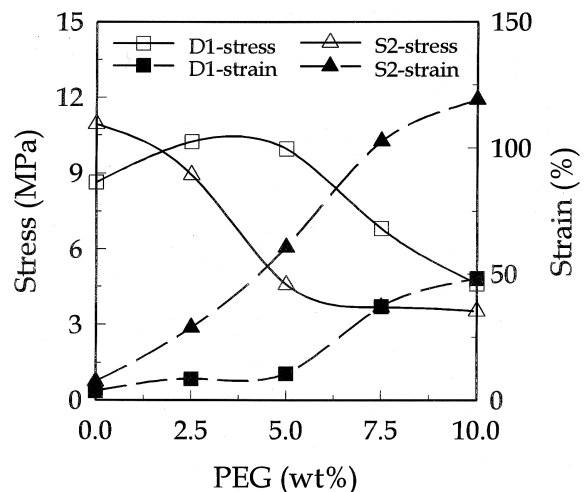

Figure 7 Effect of PEG addition on the tensile stress and strain to failure of the green tapes cast from L1 slips.

D1 tapes appear to be delayed by a "phase lag" of approximately 5 wt % relative to those of S2 tapes.

Basically, the stress variation conforms with the well-known effect: PEG of a suitable amount would depress

the interaction between PVA chains and so reduce the friction, while the long chains are forced to glide over each other. Hence, the tensile strength of green tapes, which the PVA matrix is essentially responsible for, would decrease with increasing PEG content. The longer gliding distance for PVA, as facilitated by PEG, would concurrently produce a larger strain to failure (Fig. 7). The abnormal dip of tensile stress curve of D1 tape, as observed at 0 wt % of PEG, will be discussed in section 3.4.

The finely dispersed submicrometer particles in the S2 tapes may have a function equivalent to that of PEG molecules in reducing the tensile strength, because a large specific area of powder is available for PVA to attach to, and that would reduce the chance of contact between PVA chains themselves. Therefore, with the same apparent loading of PEG for the D1 and S2 tapes, an additional amount of effective ''plasticizer'' is anticipated in the latter. This may account for the aforementioned ''phase lag'' shift.

The typical value for rupture strengths reported on alumina green tapes are 0.4–10.7 MPa and for elongation to failure 1.2–80% [9]. Therefore, adequate mechanical properties of green tapes may be achieved in the PEG content range of 2.5–10 wt % for S2 (yield stress $\sim$ 4–9 MPa, strain to failure $\sim$ 25–120%), and 5–10 wt % for D1 (yield stress $\sim$ 5–10 MPa, strain to failure $\sim$ 10–50%).

3.4. Density of green tapes

The density of green tapes cast from slip L1 and L2 series is shown in Figs 8a and 9a. In general, the lower density of tape D1 in comparison with tape S2 may arise from (1) the voids contained inside the flocculated powders of D1 tapes, and (2) the higher packing factor of particles in the
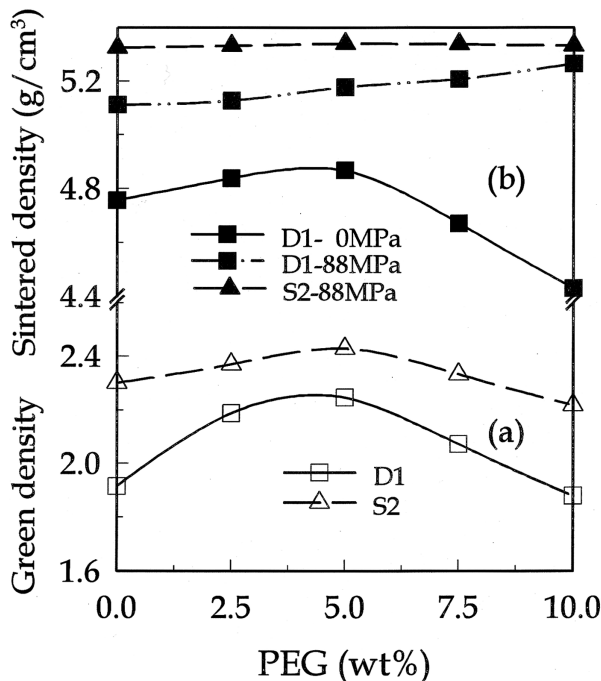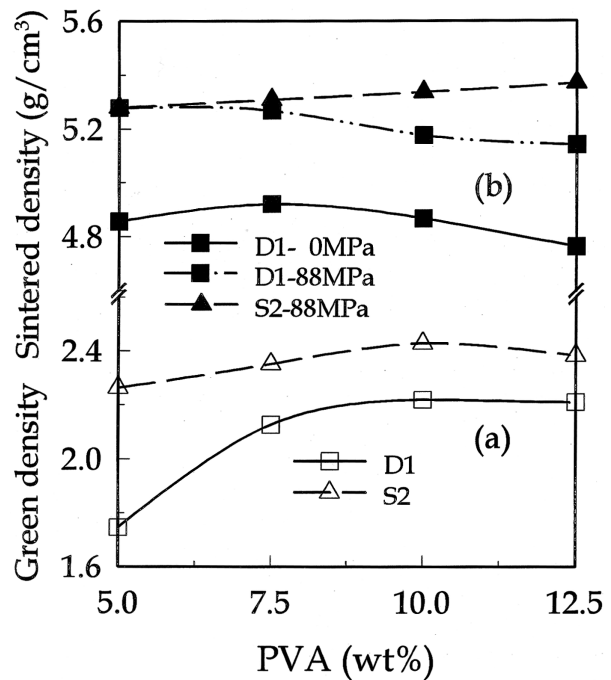

Figure 9 Effect of PVA addition on (a) the density of green tapes cast from L2 slip and (b) the density of substrates (prepared from the previous tapes) sintered for 4 h.

S2 tapes because of the two-mode particle size distributions (Fig. 3b).

In this study, a low shear rate ($< 10\,\mathrm{s}^{-1}$) of slip casting was adopted to prepare thick tapes. At such a shear rate, the high viscosity occurring in the L1 slip without PEG (see Fig. 5a) would make particle arrangement highly inhomogeneous and cause a high volume fraction of voids of the tapes (or a poor tape density, as seen in Fig. 8a). It is noted that the highly porous tape structure would give a smaller effective cross-section during the tensile-stress test, and lead to the dip of tensile stress curve of D1 tape at 0 wt % of PEG (see section 3.3.).

The D1 tape density showed a significant increase as the PEG content increased from zero to 5 wt % (Fig. 8a). Assuming that the green tapes consist mainly of ceramic powder, organic materials and voids, the relationships of the tape density ρ to the mass $W (= W_{pd} + W_{org})$ and volume $V (= V_{pd} + V_{org} + V_{vd})$ are: $\rho = W/V$ and $\Delta\rho/\rho = \Delta W/W \Delta V/V$. Then, for a PEG content change of 5 wt %, the mass increase is $\Delta W/W \approx 0.08$, and the associated change of D1 tape density is $\Delta\rho/\rho \approx 0.17$, giving $\Delta V/V \approx 0.09$. (To make the calculation on $\Delta W/W$ more transparent, W_{pd} is set equal to 50 units; W_{PVA} and ΔW_{PEG} are 10 and 5 units, respectively).

The negative volume expansion suggests a considerable decrease of voids, in addition to the reduction due to the occupation of void space by the added PEG. This decrease in voids may arise from the better fluidity of slip brought about by the added plasticizer, which helps particle rotation and improves the accommodation of particles (reducing interstitial voids) in the tapes during the slip casting. From this, the D1 tapes benefit, notably because of their initial lower packing factor of particles. In the same PEG content range, we have $\Delta\rho/\rho \approx 0.06$, $\Delta W/W \approx 0.08$ and $\Delta V/V \approx 0.02$ for S2 tape based on the similar calculation. The slight positive volume expansion indicates that the density increase may come from the

Figure 8 Effect of PEG addition on (a) the density of green tapes cast from L1 slip and (b) the density of substrates (prepared from the previous tapes) sintered for 4 h.

filling of voids with PEG rather than the improved accommodation of particles.

As the PEG loading varies from 5 to 10 wt % ($\Delta W/W \approx 0.08$), the decline in S2 tape density shown in Fig. 8a is $\Delta\rho/\rho \approx 0.09$, leading to $\Delta V/V \approx 0.17$. The volume change is approximately consistent with the predicted volume expansion (≈ 0.19) brought about by the 5 wt % gain of PEG. The expansion is estimated by taking a powder density $\sim 5\,\mathrm{g\,cm^{-3}}$, PVA and PEG densities $\sim 1.2\,\mathrm{g\,cm^{-3}}$ and a negligible volume fraction of voids. However, in the same range, the D1 tape density shows a rapid decrease $\Delta\rho/\rho \approx 0.16$, implying $\Delta V/V \approx 0.24$. The higher expansion than predicted above indicates an increase of void fraction in the tapes, which is probably due to the decreasing binding strength of PVA to the particles and consequently the poor packing of particles. Since the PEG molecules at such a high concentration may inhibit PVA chains in addition to the cross-linking, from their bonding to the particles.

On the other hand, increasing PVA content may strengthen the binding between particles and reduce their interdistances, and so enhance the tape density effectively, as seen in the PVA content range 5–10 wt % for those tapes cast from slip L2 series (Fig. 9a). Beyond that range, however, the density does not show a rapid decline as in the case of adding PEG. The constant density seems to be a balance between the volume expansion effect and the reinforced binding strength, both provided from the added PVA.

3.5. Density of sintered substrates

The sintered density of the substrates prepared from various tapes are shown in Figs 8b and 9b. For comparison, the figures also include the density of substrates D1 without lamination pressing (0 MPa), which shows that the D1 density gain through the sintering alone decreases with the amount of organic materials added. The variation of the gain is attributed to the increasing voids left after the burnout of the organic materials.

The beneficial effect of pressing on the substrate density is remarkable, indicating the significant improvement of particle packing in the green laminates after pressing. The density of the D1 substrate subjected to lamination pressing shows a monotonic increase with PEG loading, a trend distinct from that without pressing (Fig. 8b). This may be accounted for by: (1) PEG reduced the viscosity of plastic flow during the pressing, aiding the particles to reach an optimized packing. (2) PEG liquid, because of its small molecule size, was squeezed out of the laminates during the pressing, leading the final PEG content being a constant low level in the laminates, independent of its initial loading in the tapes. On the other hand, there is no such characteristic, similar to (1) and (2), associated with the PVA, hence the density of D1 substrates appears to decrease with the PVA content (Fig. 9b).

The two-mode particle size for S2 tapes allows the powder arrangement, after pressing, to produce a high packing factor without large voids, so not critically relying on the assistance of PEG. Therefore, a constant

high density ($\rho \sim 5.33\,\mathrm{g\,cm^{-3}}$) of S2 substrates results, as shown in Fig. 8b. The slight decrease in the density of S2 substrates with a low PVA content (Fig. 9b) may originate from the low binding force and, consequently, the loose powder packing of the tapes.

3.6. Microstructures and compositions of substrates

The densities of green tapes and substrates, as discussed in the above sections, depend strongly on the choice of the dispersant. Apparently, S2 exhibits superior dispersion effects and yields the higher density as measured. However, their influence is not confined to the specimen density only.

XRD studies show that the substrates D1 and S2 consist of $BaLa_2Ti_4O_{12}$ (BLT_4) main phase; and a minor phase of $Ba_4Ti_{13}O_{30}$ (B_4T_{13}) is only detected in the D1 substrates (Fig. 10a and b). The crystallinity of D1 substrates is higher than that of S1 substrates in view of their peak intensity difference. The as-measured full width at half maximum (FWHM) of the XRD main peak (5 1 1) of substrates D1 and S2 is 0.248° and 0.275° when sintered for 0.5 h; and 0.148° and 0.265° when sintered for 4 h.

Observations of typical microstructures of D1 and S2 substrates (e.g. those prepared from slip L2 with 7.5 wt % of PVA) using SEM reveal measurable minor phase in the former (the dark regions), but it is rare in S2 substrates (Fig. 11a to d). The major phase appears in the shape of short rods and the minor phase forms into equiaxial grains. The measured compositions of the major phase BLT_4 are listed in Table II, which shows that S2 ones remained close to a stoichiometric ratio during the sintering, and the D1 case has a substantial replacement of La for Ba ions. In the previous study on $BaO \bullet La_2O_3 \bullet 4.7TiO_2$ ceramics, samples in a cylindrical shape sintered at 1300 °C for 4 h have microstructures with BLT_4 and B_4T_{13} phases as well as

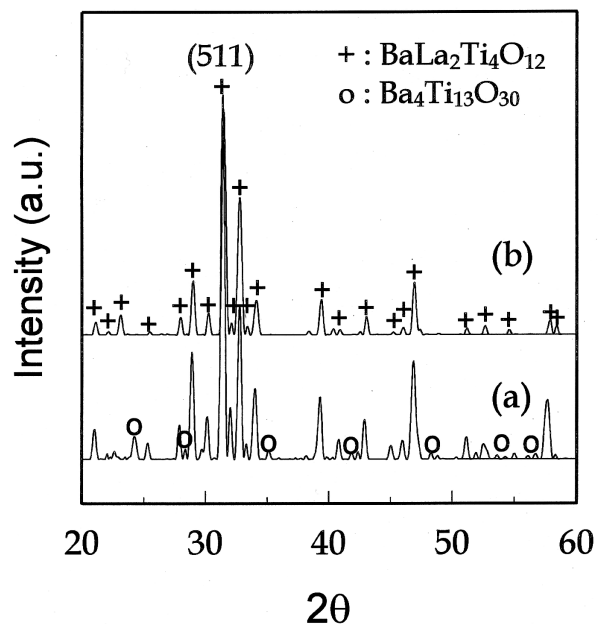*Figure 10* XRD patterns of (a) D1 and (b) S2 substrates sintered for 4 h, showing (a) BLT_4 and B_4T_{13} phases and (b) only BLT_4 phases.

TABLE II Compositions of the major phase $(Ba,La)La_2Ti_4O_{12}$ in D1 and S2 substrates sintered at 1300°C for 0.5 h and 4 h

Substrate	Sintering time (h)	Ba	La	Ti
D1	0.5	0.87	2.09	4
	4.0	0.84	2.14	4
S2	0.5	0.92	2.02	4
	4.0	0.91	2.06	4

an abundant substitution of La for Ba ions in the former [12], similar to that of D1 substrates.

The distinct microstructures present in the substrates D1 and S2 may arise from different thermal characteristics of the dispersant used. During the burnout stage, the dispersant D1, vanished together with other organic materials, because of its low decomposition temperature ~ 500°C. However, inorganic dispersant S2 (melting point ~ 900°C) was found to be present until the initial stage of sintering. A notable concentration of Na^+ ions was detected on the grain boundaries of substrates S2 (sintered for 0.5 h, Fig. 12), where a liquid phase S2 is seen surrounding the grains. The liquid vanished entirely after sintering for 4 h. Detailed microstructures of the substrates D1 and S2 are shown in Fig. 13a to d.

Both the grain size and density of S2 substrates ($\rho \sim 4.75$ g cm^{-3}) are found smaller than that of D1 substrates (5.0 g cm^{-3}) in the early stage of sintering (for 0.5 h). The liquid S2 on the grain boundaries seemed to act as an inhibitor to the intergrain diffusion and to hinder the densification process. This might arise from the negligible solubility of the ceramics in the liquid S2, as evidenced by the concentration profile measured at their contact region (Fig. 14) where drops of S2 liquid lying on a pure ceramics bulk was held at 1300°C for 0.5 h. Apparently, the liquid would not be a good medium for the ion diffusion among ceramics grains and provides no function to facilitate the sintering process, and it may also inhibit the formation of second phase in the S2 substrates.

3.7. Microwave dielectric properties of substrates

The microwave dielectric properties (measured at 1 GHz) of the substrates are listed in Table III.
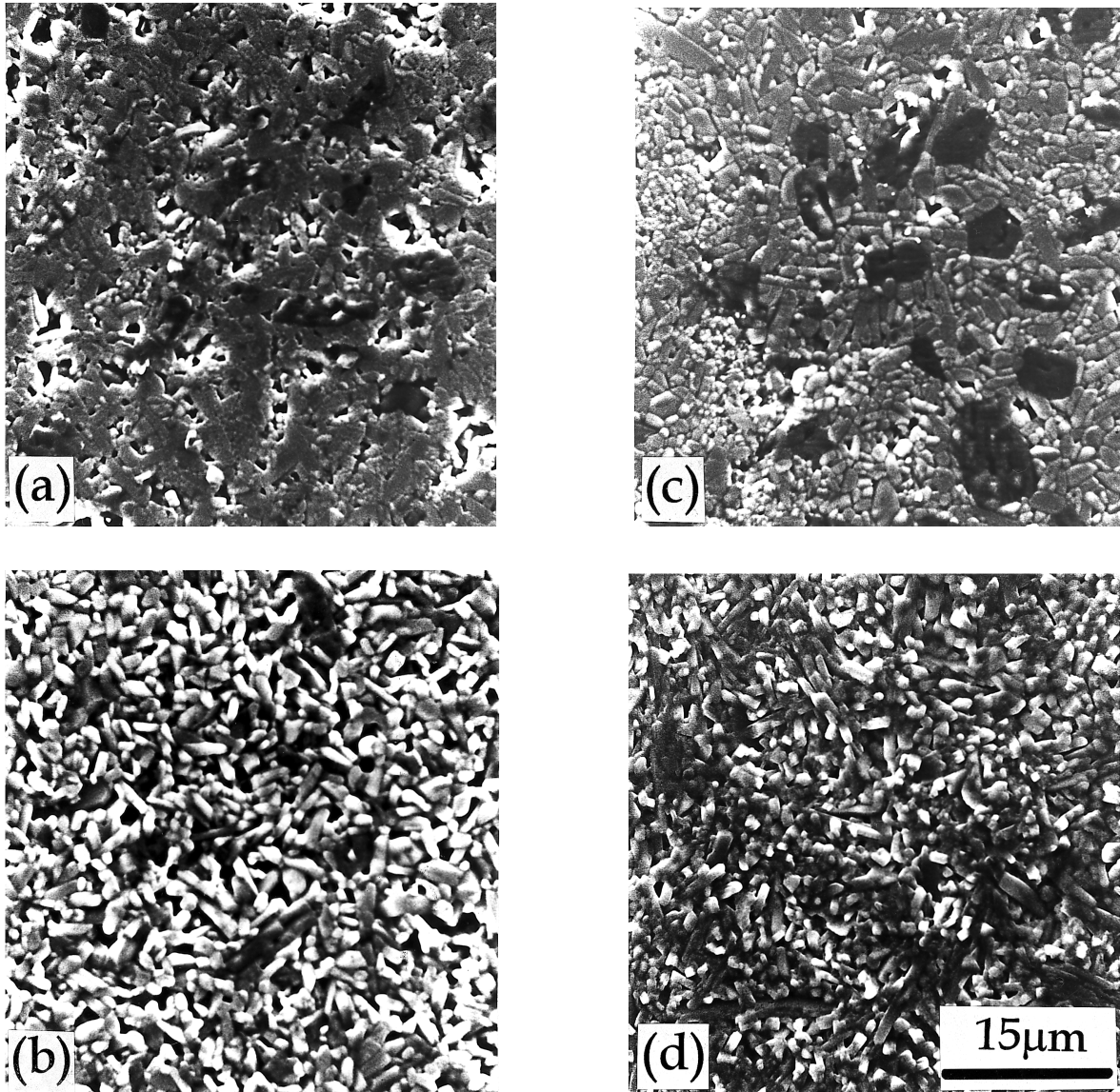

Figure 11 SEM micrographs of (a) D1 and (b) S2 substrates sintered for 0.5 h; and (c) D1 and (d) S2 substrates sintered for 4 h, showing the major phase (BLT$_4$) in the shape of short rods and the equiaxial dark grains of minor phase (B$_4$T$_{13}$).
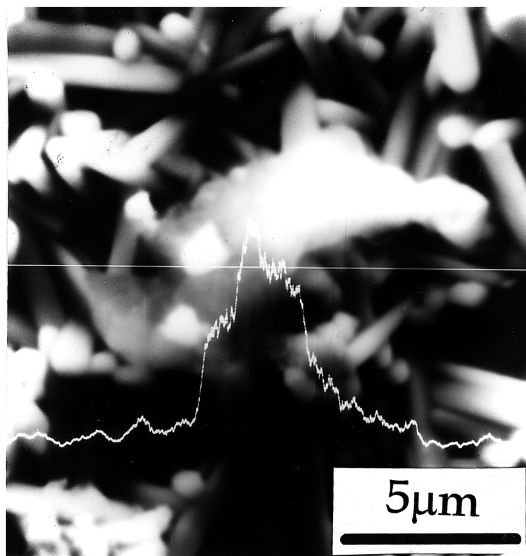
Figure 12 WDS analysis on the S2 substrates sintered for 0.5 h, showing a Na concentration profile across the grains.

TABLE III Microwave dielectric properties of D1 and S2 substrates sintered at 1300 °C for 0.5 h and 4 h

Substrate	Sintering time (h)	ε	Q
D1	0.5	76	1890
	4.0	84	1500
S2	0.5	62	2160
	4.0	66	2500

Substrates S2 show a lower dielectric constant (ε) and a higher quality factor (Q) than that of substrates D1. All these properties improve with the sintering except the quality factor of D1 samples.

Before the detailed discussions on the complex microwave propereties, an approximate estimation on value of BLT_4 and B_4T_{13} phases is attempted here based on the empirical equation: $\ln \varepsilon = v_1 \ln \varepsilon_1 + v_2 \ln \varepsilon_2$, where v_1 and v_2 are the volume fractions of the constituent phases. For substrates D1, the measured , v_1 and v_2 are 84, 0.85 and 0.15; and for the cylindrical sample, they are 93, 0.91 and 0.09 [12], where 1 and 2 refer to the major and minor phases. Substituting the
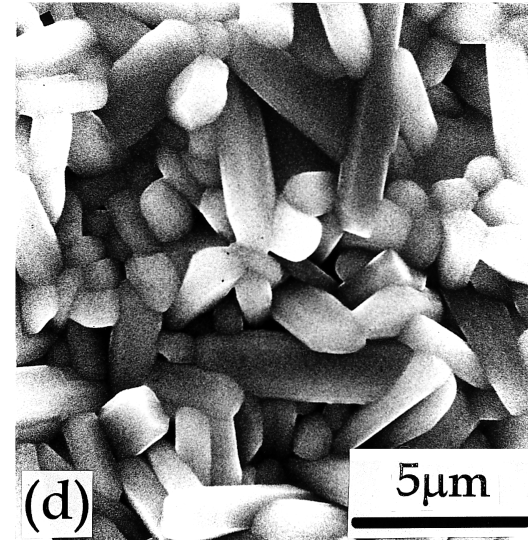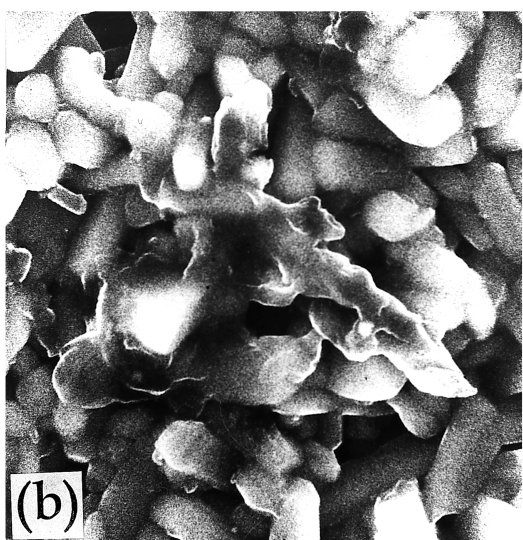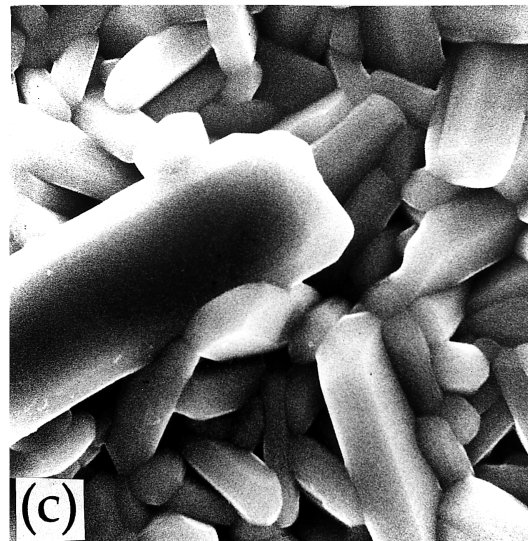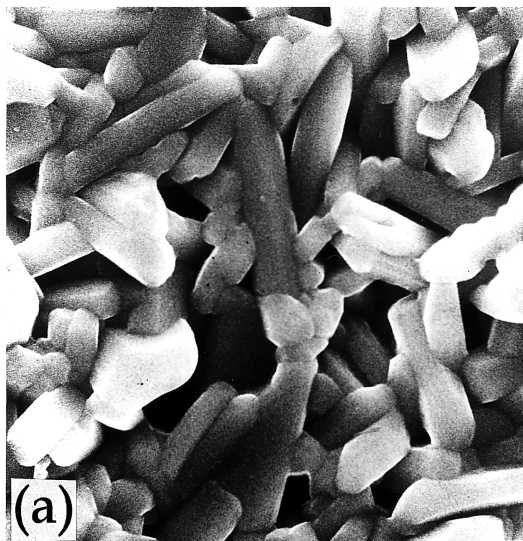

Figure 13 SEM micrographs of Fig. 11 with a higher magnification, showing the grain growth in S2 substrates was inhibited by the presence of S2 liquid phase in-between the grains.
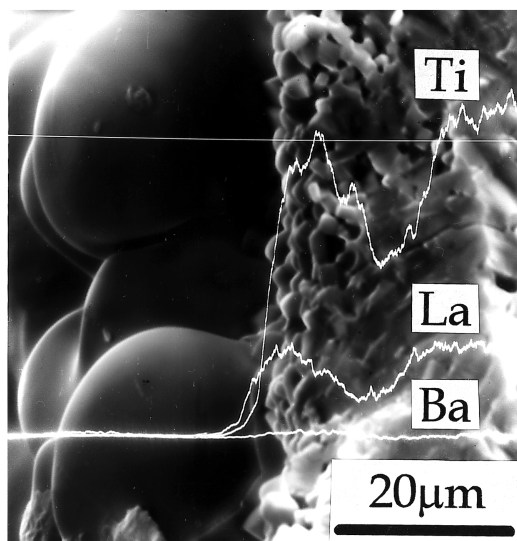
416

Figure 14 Concentration profiles of Ba, La and Ti ions near the contact region of S2 liquid and a pure ceramic, showing the negligible solubility of the ceramic in the liquid S2.

relevant data into the above equation results in dielectric constants: 108 and 20 for the main and minor phases, respectively. The former is found to be close to the reported $\varepsilon(=109)$ on material $BaLa_2Ti_4O_{12}$ [16], indicating a weak dependence of the dielectric constant of BLT_4 on the replacement of La for Ba ions.

The lower volume fraction of low-dielectric B_4T_{13} phase in the substrates D1 sintered for 0.5 h compared with that for 4 h (see Fig. 11a and c) may enhance the value of the former, but the higher porosity and the lower degree of crystallization appear to be more important factors, producing a smaller dielectric constant. The same considerations may be applied to the case of substrate S2, which achieved the same density as D1 substrates for 4 h sintering and was without B_4T_{13} phase. Nevertheless, the insufficient crystallization due to the intergranular S2 liquid makes the value comparatively low.

However, the better crystallization assumed in the substrates D1 (with a less specific homogeneous grain boundary area and a lower intragrain defect concentration) did not give a higher quality factor, as expected. The source dominating the dielectric loss is likely to be the heterogeneous grain boundaries between the major and minor phases, which usually contain concentrated defects inducing a significant loss. The development of the minor phase with the sintering time, as observed in the microstructure evolution of the D1 substrates (Fig. 11a to c), is found to be consistent with the abnormal decline of the Q value when the sintering time extends from 0.5 to 4 h. Also, the absence of minor phase in the S2 substrates allows them to be free from the major loss and they have a quality factor higher than that of D1 substrates; and their Q value could be improved with the crystallization or the sintering time (see Table III). The S2 liquid present in the substrates (sintered for 0.5 h) may contribute to the loss too, but it does not seem to be a major source.

4. Conclusion

In an aqueous-based slip of $BaO \bullet La_2O_3 \bullet 4.7TiO_2$ ceramic powder, dispersant $Na_4P_2O_7$ (S2) shows a better dispersion effect than that of $CH_3(CH_2)_4So_3Na$ (D1). Adding suitable quantities of binder PVA and plasticizer PEG, the slips show adequate rheological behaviour and yield appropriate mechanical properties of green tapes. The two-mode particle size distribution induced by dispersant S2 is helpful to produce a green tape density higher than that of D1 tapes. The lamination pressing produced enhanced densification of sintered substrates effectively. The substrates D1 have highly crystallized microstructures consisting of a major phase BLT_4 and a minor phase B_4T_{13}, which give a high dielectric constant and low quality factor. The S2 substrates have under-developed microstructures due to the S2 liquid remaining on the grain boundaries until the early stage of the sintering. The liquid has a negligible solubility of the ceramics and acts as an inhibitor to the intergrain diffusion, grain growth and minor phase formation. This results in a lower dielectric constant and a higher quality factor compared with that of D1 substrates.

References

1. D. J. SHANEFIELD, P. T. MORZENTI and R. E. MISTLER, *Ceram. Bull.* **53** (1974) 564.
2. D. COOPER, P. G. NEWLAND and F. W. SHAPLEY, ''The Development of High-Quality Alumina Substrates'', edited by P. Vincenzini (Elsevier, Amsterdam, Netherlands, 1987) p. 1549.
3. R. E. MISTLER, *Ceram. Bull.* **69** (1990) 1022.
4. E. P. HYATT, *ibid.* **65** (1986) 637.
5. J. TAKAHASHI, T. IKEGAMI and K. KAGEYAMA, *J. Am. Ceram. Soc.* **74** (1991) 1868.
6. J. P. GUHA, *ibid.* **74** (1991) 878.
7. K. FUKUDA, I. FUJII, R. KITOH, Y. OHO and I. AWAI, *Jpn. J. Appl. Phys.* **32** (1993) 1712.
8. J. TAKAHASHI, K. KAGEYAMA and K. KODAIRA, *ibid.* **32** (1993) 4327.
9. D. HOTZA and P. GREIL, *Mater. Sci. Eng. A* **202** (1995) 206.
10. Z.-C. CHEN, T. A. RING and J. LEMAITRE, *J. Am. Ceram. Soc.* **75** (1992) 3201.
11. N. USHIFUSA and M. J. CIMA, *ibid.* **74** (1991) 2443.
12. C. C. LEE and P. LIN, To be published in *Jpn. J. Appl. Phys.* **37** (1998).
13. N. J. DAMASKOS and B. J. KELSALL, *Microw J.* **38** (1995) 140.
14. R. J. HUNTER, ''Zeta Potential in Colloid Science'' (Academic, New York, 1981) p. 224.
15. C. W. NIES and G. L. MESSING, *J. Am. Ceram. Soc.* **67** (1984) 301.
16. K. C. JAMES RAJU, V. SIVASUBRAMANIAN, R. PRAGASAM, B. VISWANNTHAN and V. R. K. MURTHY, *J. Appl. Phys.* **74** (1993) 1968.